Understanding cardiac alternans: A piecewise linear modeling framework

R. Thul[a)] and S. Coombes[b)]
*School of Mathematical Sciences, University of Nottingham, Nottingham,
Nottinghamshire NG7 2RD, United Kingdom*

Cardiac alternans is a beat-to-beat alternation in action potential duration (APD) and intracellular calcium (Ca^{2+}) cycling seen in cardiac myocytes under rapid pacing that is believed to be a precursor to fibrillation. The cellular mechanisms of these rhythms and the coupling between cellular Ca^{2+} and voltage dynamics have been extensively studied leading to the development of a class of physiologically detailed models. These have been shown numerically to reproduce many of the features of myocyte response to pacing, including alternans, and have been analyzed mathematically using various approximation techniques that allow for the formulation of a low dimensional map to describe the evolution of APDs. The seminal work by Shiferaw and Karma is of particular interest in this regard [Shiferaw, Y. and Karma, A., "Turing instability mediated by voltage and calcium diffusion in paced cardiac cells," Proc. Natl. Acad. Sci. U.S.A. **103**, 5670–5675 (2006)]. Here, we establish that the key dynamical behaviors of the Shiferaw–Karma model are arranged around a set of switches. These are shown to be the main elements for organizing the nonlinear behavior of the model. Exploiting this observation, we show that a piecewise linear caricature of the Shiferaw–Karma model, with a set of appropriate switching manifolds, can be constructed that preserves the physiological interpretation of the original model while being amenable to a systematic mathematical analysis. In illustration of this point, we formulate the dynamics of Ca^{2+} cycling (in response to pacing) and compute the properties of periodic orbits in terms of a stroboscopic map that can be constructed without approximation. Using this, we show that alternans emerge via a period-doubling instability and track this bifurcation in terms of physiologically important parameters. We also show that when coupled to a spatially extended model for Ca^{2+} transport, the model supports spatially varying patterns of alternans. We analyze the onset of this instability with a generalization of the master stability approach to accommodate the nonsmooth nature of our system. © *2010 American Institute of Physics*. [doi:10.1063/1.3518362]

Beat-to-beat patterns of alternating activity seen in whole heart electrocardiograms are often taken as a sign of an abnormal rhythm that may lead to sudden cardiac death. The initiation and maintenance of such pathological cardiac *alternans* can be linked to dynamics at the single cell level. Here, it also manifests itself as a beat-to-beat alternation, although this time in the duration of action potentials. These electrical spikes of activity ultimately control the contraction of heart muscle fibers. Because of the known link between cellular alternans and cardiac arrhythmias, understanding the mechanism of their generation is vital for developing preventative clinical treatments. Experiments have shown that cellular alternans arise from an interplay of membrane voltage dynamics and intracellular Ca^{2+} cycling. However, these studies have not been able to fully unravel the relative contributions of these distinct electrical and chemical signaling pathways to the development of alternans. Thus, modeling is ideally suited to determine the roles that voltage and Ca^{2+}-dependent coupling play in generating regular and irregular rhythms in the heart. Here, we develop the analysis of an existing model of this process and show how increased insight into the alternans phenomenon can be obtained with a systematic reduction of the nonlinearities to piecewise linear forms. This allows for the explicit construction of periodic orbits and a determination of their stability in terms of a set of switching times. Importantly, the conditions for a period-doubling bifurcation, leading to alternans, can be identified in terms of physiologically important parameters. Moreover, we show that tissue level models, constructed by coupling such cells, show spatiotemporal patterns of alternans that can be understood with a mathematical generalization of techniques used to study instabilities of synchronized states in linearly coupled oscillator networks.

I. INTRODUCTION

Understanding the mechanisms of cardiac arrhythmia is of obvious importance in the prediction and prevention of sudden cardiac death. Interestingly, many ventricular arrhythmias have been linked to single cell myocyte dynamics [see Laurita and Rosenbaum (2008) for a recent review]. Thus, within the physiological modeling community, there is a great deal of emphasis on developing single cell models for cardiac rhythmogenesis. In healthy tissues, single cell rhythmic activity underlies whole heart cell muscle contraction—

a)Electronic mail: ruediger.thul@nottingham.ac.uk.
b)Electronic mail: stephen.coombes@nottingham.ac.uk.

20, 045102-1

the heartbeat. Cardiac excitation-contraction coupling is the process that links electrical excitation of the heart cells to the production of contraction. It is caused by the passage of an action potential over a myocyte (Bers, 2002). The resultant change in membrane potential activates voltage-operated calcium (Ca^{2+}) channels (mainly L-type Ca^{2+} channels) which triggers a calcium signal. This in turn evokes a more substantial Ca^{2+} release from closely apposed ryanodine receptor (RyR) clusters on the sarcoplasmic reticulum (SR) (an intracellular Ca^{2+} store) via Ca^{2+}-induced Ca^{2+} release. Such a localized transient response seen in the cell cytosol, from a cluster of RyRs, is often called a Ca^{2+} spark (Cheng *et al.*, 1993). For ventricular myocytes, action potential-evoked Ca^{2+} signals take the form of homogeneous global increases, reflecting the spatial and temporal summation of many Ca^{2+} sparks (Cannell *et al.*, 1995). It is precisely these global signals that activate the contractile machinery of the cell (comprising actin and myosin myofibrils). On a beat-to-beat basis, the strength of contraction is proportional to the amount of Ca^{2+} released from the SR, which in turn is critically dependent on the amount of Ca^{2+} entering through L-type Ca^{2+} channels. For repetitive behavior to be possible, Ca^{2+} must be removed from the cell via a Na–Ca exchanger (NCX) to balance that entering the cell via L-type Ca^{2+} channels as well as pumped back into the SR to be available for release at the next beat. Thus, pathological behaviors can arise if these processes are interrupted or if an action potential arrives before sufficient store-refilling occurs. As a result, cardiac alternans can develop in response to periodic electrical pacing in which the peak cytosolic Ca^{2+} concentration alternates from beat-to-beat. Moreover, the detailed form of such alternans is influenced by the coupling of membrane voltage and intracellular Ca^{2+} concentration. Notably, rises in cytosolic Ca^{2+} can affect Ca^{2+}-dependent membrane currents which control the shape of the action potential.

Models of the heart and heart cells have been actively developed since the 1960s. These were initially based on the current balance ideas of Hodgkin and Huxley and were extended in the 1980s to include Ca^{2+} dynamics. In recent years, such cellular models have been incorporated into anatomically detailed tissue and organ models. For a recent discussion, we refer the reader to Noble (2004). Using the techniques of computational cell biology, much have been learned about the normal and pathological behaviors of myocytes and cardiac tissues from the study of models. Most famous among these are the models of Noble (1962), Beeler and Reuter (1977), and Luo and Rudy (1991). For a current comprehensive list of cardiac cell models, we direct the reader to Fenton and Cherry (2008). In particular, the analysis of the Shiferaw–Karma model (Shiferaw *et al.*, 2003), with a mixture of numerical simulation and mathematical analysis, has shed much light on the mechanism for alternans. However, the nonlinear nature of this (and indeed all cardiac cell models) has meant that mathematical analysis has only been possible with various assumptions, such as the slaving of one model variable to another, which may not always hold true. In the absence of a general set of mathematical techniques for understanding nonlinear models, it is often convenient to first develop a simpler piecewise linear

(PWL) caricature that can be explicitly analyzed. For example, in neuroscience the model of McKean (1970) of an excitable cell is one in which the dynamics is broken into simpler linear pieces (essentially by replacing the cubic nullcline of the FitzHugh–Nagumo model with a PWL function). In this paper, we adopt this philosophy and develop a mathematically tractable version of the Shiferaw–Karma model.

In Sec. II, we review the Shiferaw–Karma model and introduce its PWL caricature. Numerical simulations are used to highlight the excellent correspondence of the two models in response to periodic pacing. Next, in Sec. III, we construct the periodic orbits of the PWL model, and show how they can be analyzed in terms of a set of switching times. Importantly, we show how to determine stability, and use this approach to identify physiological parameter regimes that can support a period-doubling bifurcation. The onset of alternans as predicted by this instability is shown to be in excellent agreement with numerical simulations. This approach is extended to the network level in Sec. IV for cells coupled by their bulk cytosolic Ca^{2+} concentration differences. We develop a generalization of the Pecora and Carroll (1998) master stability calculation, to handle switching times, to determine the instability point of the synchronized state. Once again, the predicted onset of spatiotemporal alternans is shown to be in excellent agreement with numerical simulations. Finally, in Sec. V, we discuss the results of our analysis as well as the natural extensions of the work in this paper.

II. THE MODEL

Experiments to date are inconclusive about the relative contributions of membrane voltage and intracellular Ca^{2+} handling to the development of alternans (Qu and Weiss, 2007; Jordan and Christini, 2007). Thus, modeling is ideally suited to determine the roles that voltage and Ca^{2+}-dependent coupling play in generating regular and irregular rhythms in cardiac myocytes, thereby providing further insights into the mechanism of alternans. Here, we will focus on the class of models where the shape of the membrane potential V is fixed, i.e., V is a function of time only and acts as a drive to the intracellular Ca^{2+} dynamics. We base our analysis on the Shiferaw–Karma model developed by Shiferaw *et al.* (2003), which describes the Ca^{2+} dynamics in four intracellular compartments and the release current I_r from the SR into the cytosol. We now give a brief description of this model.

A. Shiferaw–Karma model

The cytoplasm is divided into the subsarcolemmal space and the bulk, while in the SR the total Ca^{2+} concentration and the Ca^{2+} concentration in the unrecruited junctional SR (JSR) are tracked. The unidirectional coupling from the membrane potential to the Ca^{2+} cycling occurs through the L-type Ca^{2+} channel and the NCX. Upon depolarization of the plasma membrane, L-type Ca^{2+} channels open and translocate Ca^{2+} from the extracellular space into the dyadic cleft. The ensuing rise of the subsarcolemmal Ca^{2+} concentration triggers the release of Ca^{2+} from the SR, which in turn in-

creases the Ca^{2+} concentration in the dyadic cleft. This positive feedback of the L-type current on the Ca^{2+} liberation from the SR is modulated by the Ca^{2+} load of the unrecruited JSR in a strongly nonlinear fashion. Experiments have revealed a cubic dependence of the Ca^{2+} released from the SR on the SR Ca^{2+} load (Trafford *et al.*, 2001). While the membrane potential is the key for opening L-type Ca^{2+} channels, the deactivation occurs through a combination of voltage gates that respond to membrane repolarization and Ca^{2+} sensors that are activated at large subsarcolemmal Ca^{2+} concentrations (Matthes and Herzig, 2010). The main role of the NCX is to extrude Ca^{2+} from the cytosol to the extracellular space to achieve low resting levels of the diastolic Ca^{2+} concentration. The strength of the NCX current depends on both the subsarcolemmal Ca^{2+} concentration and the membrane potential. The above biological features are captured with the following set of five ordinary differential equations:

$$\frac{dc_s}{dt} = \beta(c_s)\left[\frac{v_i}{v_s}\left(I_r - \frac{c_s - c_i}{\tau_s} - I_{CaL}\right) + I_{NaCa}\right],$$

$$\frac{dc_i}{dt} = \beta(c_i)\left[\frac{c_s - c_i}{\tau_s} - I_{up}\right],$$

$$\frac{dc_j}{dt} = -I_r + I_{up}, \qquad\qquad (1)$$

$$\frac{dc_j'}{dt} = \frac{c_j - c_j'}{\tau_a},$$

$$\frac{dI_r}{dt} = -gI_{CaL}Q(c_j') - \frac{I_r}{\tau_r}.$$

Here, $(c_s, c_i, c_j, c_j', I_r)$ denote the subsarcolemmal Ca^{2+} concentration, the cytosolic Ca^{2+} concentration, the total Ca^{2+} concentration in the SR, the Ca^{2+} concentration in the unrecruited JSR, and the release current from the SR into the cytosol. The volumes of the intracellular space and the bulk cytosol are denoted by v_s and v_i, respectively. The Ca^{2+} current through the L-type Ca^{2+} channel is given by $I_{CaL}=I_{CaL}(c_s,V)$, that through the NCX is given by $I_{NaCa}=I_{NaCa}(c_s,V)$, and that through the Ca^{2+} pumps (from the cytosol to the SR) is given by $I_{up}=I_{up}(c_i)$. The diffusive currents between the subsarcolemmal space and the bulk cytosol as well as between the two SR Ca^{2+} concentrations are controlled by the time constants τ_s and τ_a, respectively. The time constant τ_r corresponds to the lifetime of a Ca^{2+} spark and g is the release current strength. The function Q describes the load-release function. Note that this is a PWL function of c_j' and switches at prescribed threshold values of c_j'. Details of all currents and coefficients are listed in Appendix A. The model (1) is stimulated by clamping the voltage variable V to some chosen functions of time. We take this to be a T_p-periodic waveform that mimics the shape of realistic cardiac action potentials with values between V_{min} and V_{max}.

Given that the Ca^{2+} concentration in the four compartments of the Shiferaw–Karma model decays toward resting values in the absence of an action potential (V clamped at

V_{min}), the combined positive and negative feedback of the membrane potential on the Ca^{2+} cycling significantly shapes the Ca^{2+} response. Figures 1 and 2 show the typical traces of all dynamic components in the Shiferaw–Karma model for pacing periods $T_p=1$ s and $T_p=0.27$ s, respectively. While there are regular period 1 oscillations at the smaller pacing frequency, the dynamics undergoes a period-doubling bifurcation as the frequency is increased. The regular alternation of large and small peaks in the Ca^{2+} concentrations is known as Ca^{2+} alternans. The absolute values of the local maxima as well as the difference between successive peak values depend on the pacing frequency. Note that these alternans occur although the action potential duration (APD) remains constant.

To gain a deeper understanding of the emergence of alternans, we now introduce a PWL approximation of the Shiferaw–Karma model that is amenable to a full mathematical analysis.

B. PWL model

The PWL model possesses the same structure as the original Shiferaw–Karma model, i.e., we consider the same five dynamical variables, and the coupling between them occurs through the same currents. The main changes concern the specific form of the currents, most notably of those through the L-type Ca^{2+} channel and the NCX. For the former, we make use of the fact that the L-type Ca^{2+} channel activates to a voltage-dependent maximum almost instantaneously upon strong depolarization and then remains open for a short period of time (see Figs. 1 and 2). Hence, we eliminate all gating variables and model the current through the L-type channel with a simple voltage-dependent switch. We set the conductance to a constant that is proportional to the maximal value of the action potential. The channel opens at the onset of the action potential, and to retain the voltage-dependent inactivation, the L-type Ca^{2+} channel is only active as long as $V \geq V_L$, where the threshold voltage $V_L = V_{max} - 1$ is chosen so as to result in a reasonable time of conductance (on the order of 5 ms). Note that a constant L-type current allows us to use the continuous load-release function Q of the original Shiferaw–Karma model given by Eq. (A2). Since the current through the NCX is a combined function of the membrane potential and the subsarcolemmal Ca^{2+} concentration, we split it into a voltage-dependent and a Ca^{2+} dependent part and write it in the form $I_{NaCa}(V,c_s) = \phi(V) - \psi(V)c_s$. The function $\phi(V)$ is quadratic in V, while $\psi(V)$ is a piecewise constant function of V that switches at the voltage level V_{NaCa}, both of which are defined in Appendix B. The values of the PWL function as well as that of V_{NaCa} are chosen such as to faithfully reproduce the NCX current of the original Shiferaw–Karma model (see bottom right panel in Fig. 2). The Shiferaw–Karma voltage clamp is derived from experimental protocols and describes the active part of the action potential with a functional dependence on time that goes as $\sqrt{1-t^2}$. For our purposes, it is more convenient to expand the square root into a superposition of cosine functions [see Eqs. (B6)–(B8)]. We only need three terms in this series to achieve a good agreement between the expan-
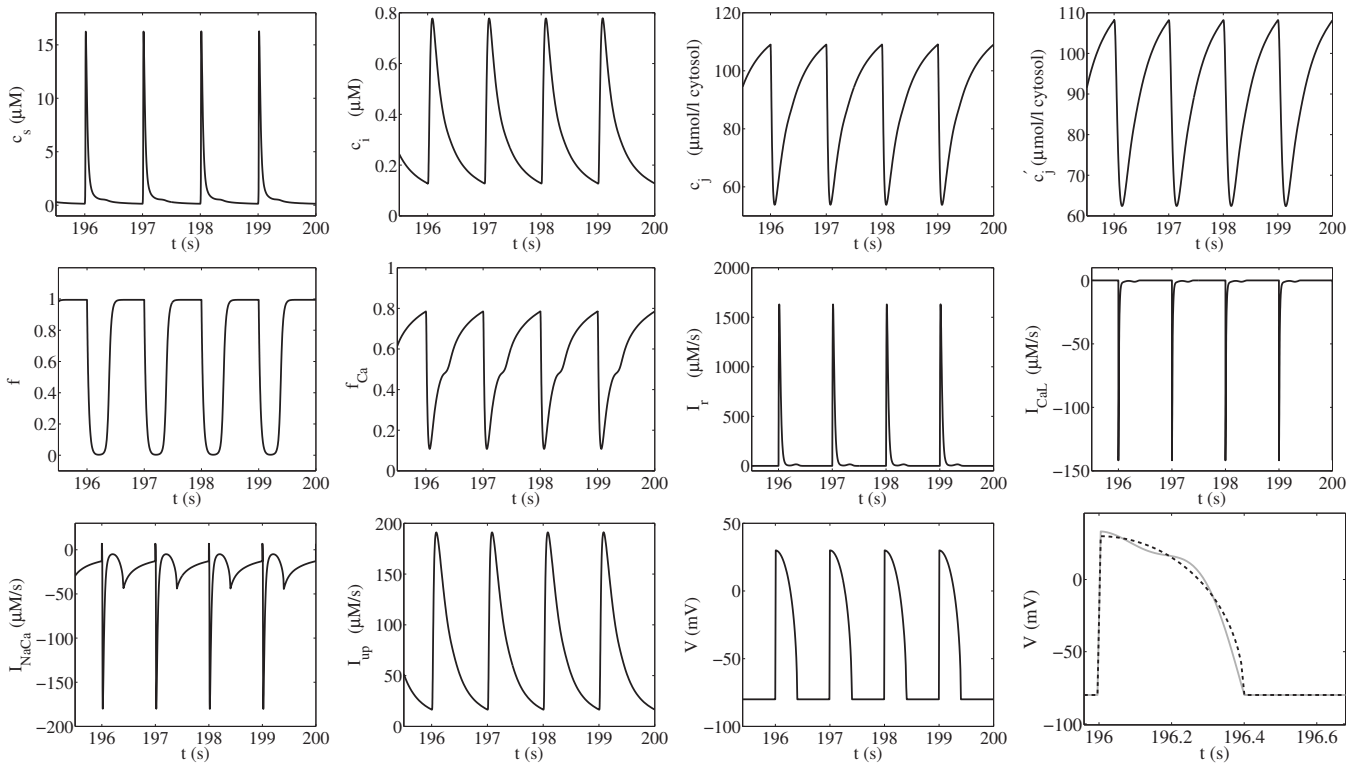
FIG. 1. Time courses of the Ca^{2+} concentration in the subsarcolemmal space (c_s), the cytosolic bulk (c_i), the total Ca^{2+} in the SR (c_j), the Ca^{2+} concentration in the unrecruited JSR (c_j'), the voltage-dependent (f) and Ca^{2+} dependent (f_{Ca}) inactivation gate of the L-type Ca^{2+} channel, the release current I_r, the L-type Ca^{2+} current I_{CaL}, the NCX current I_{NaCa}, the uptake current I_{up}, and the clamped action potential V in the Shiferaw–Karma model at a pacing period of $T_p=1$ s. The bottom right panel shows an overlay of the action potential in the Shiferaw–Karma model (dashed black line) and the PWL model (solid gray line) for $T_p=1$ s. All other parameter values as in Tables I–V.

sion and the choice of the voltage clamp in the Shiferaw–Karma model (see bottom right panel of Fig. 1). However, it is worth noting that the analysis we present below holds for an arbitrary number of terms in the cosine series so that we can approximate the original voltage clamp to any degree of accuracy. Finally, we substitute the nonlinear pump current I_{up} by a linear relationship based on earlier results (Coombes, 2001), and we replace the terms $\beta(c_s)$ and $\beta(c_i)$ with constants that lie in the range of β given by Eq. (A1). We refer the reader to Appendix B for further details of the model.

Figures 3 and 4 show the results for the PWL model at cycle lengths of $T_p=1$ s and $T_p=0.35$ s, respectively. We again find a period-doubling bifurcation as we increase the pacing frequency. The range of Ca^{2+} concentrations in all four compartments agrees well between the two models on either side of the period-doubling bifurcation. The PWL model retains the property that the total Ca^{2+} concentrations in the SR (c_j) and in the unrecruited JSR (c_j') are similar, while there is an order of magnitude difference between the cytosolic bulk and the subsarcolemmal space. Moreover, we recover the same separation of time scales in the cytosol since the Ca^{2+} concentration in the dyadic cleft decays much faster than the bulk Ca^{2+} concentration. In addition, the two luminal Ca^{2+} concentrations exhibit similar recovery time courses. The PWL approximation of the NCX current responds to an action potential with the same characteristics as the full model, such as the strong down swing at the onset of the action potential, the shoulder like structure shortly afterward, and the following dip. The bottom right panel of Fig. 2

shows a plot of I_{NaCa} for the Shiferaw–Karma model and PWL model, highlighting the good agreement between the two.

An important property of cardiac Ca^{2+} models is the existence of graded release, where the amount of Ca^{2+} that enters the cell through L-type Ca^{2+} channels and released from the SR changes with the amplitude of applied voltage pulses. Figure 5 depicts the maximum of I_{CaL} and I_r normalized to the overall maximum for test potentials of various heights. In both models, the overall maximum is achieved for test pulses up to 10 mV. An increase in the potential step leads to a decrease of the currents where I_{CaL} decays faster than I_r. For the PWL model, we only plot the current responses to test potentials larger than 10 mV because there is no inactivation mechanism for negative membrane potentials. We also found that our model reliably exhibits gain, where the amount of Ca^{2+} liberated from the SR is much larger than the amount that enters the cell through L-type Ca^{2+} channels (data not shown).

The PWL model successfully captures a wide range of properties of the original Shiferaw–Karma model. Hence, it is ideally suited to investigate cardiac Ca^{2+} dynamics in more details. We illustrate in the next section how to analytically construct periodic orbits that correspond to regular Ca^{2+} oscillations. Moreover, we determine the linear stability of these oscillations and provide analytical expressions that signal the onset of Ca^{2+} alternans via a period-doubling bifurcation.
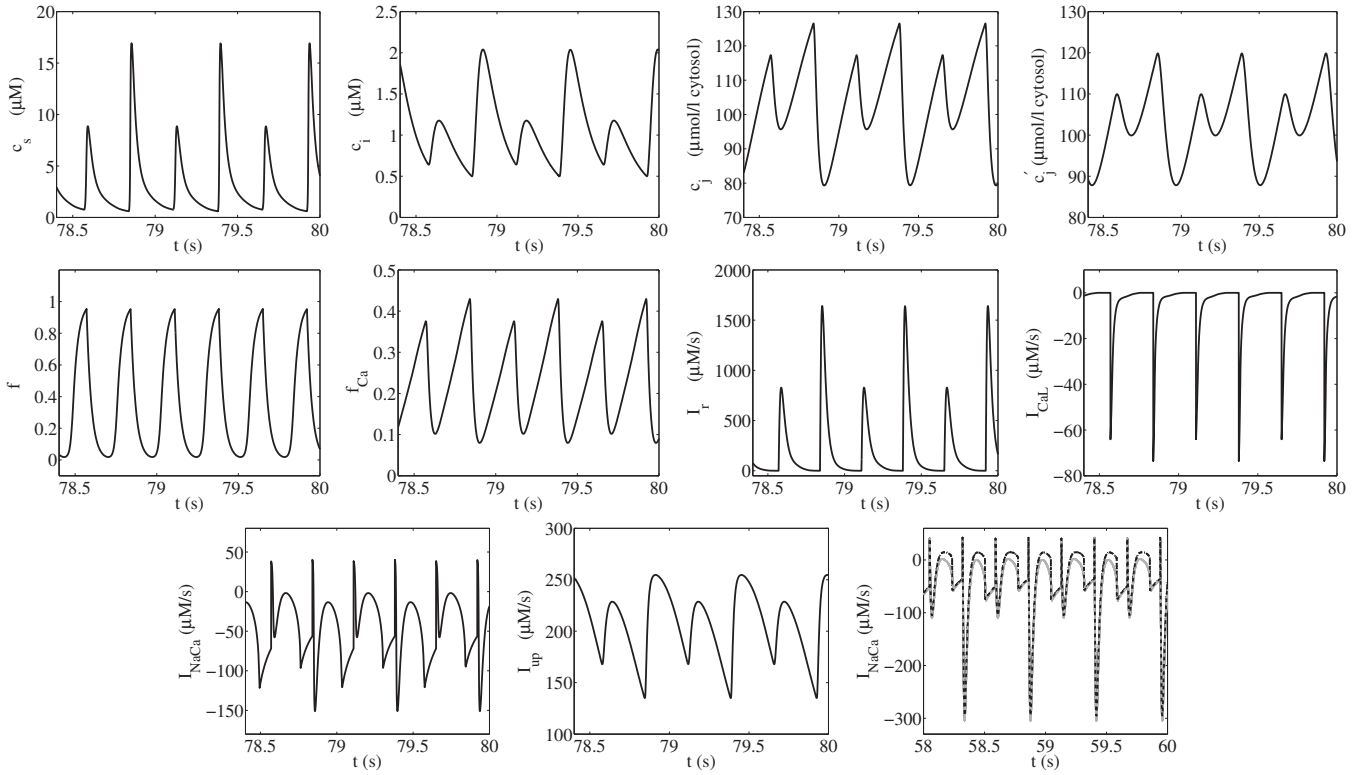
FIG. 2. Time courses of the Ca^{2+} concentration in the subsarcolemmal space (c_s), the cytosolic bulk (c_i), the total Ca^{2+} in the SR (c_j), the Ca^{2+} concentration in the unrecruited JSR (c_j'), the voltage-dependent (f) and Ca^{2+} dependent (f_{Ca}) inactivation gate of the L-type Ca^{2+} channel, the release current I_r, the L-type Ca^{2+} current I_{CaL}, the NCX current I_{NaCa}, and the uptake current I_{up} in the Shiferaw–Karma model at a pacing period of $T_p = 0.27$ s. The bottom right panel shows an overlay of the NCX current in the Shiferaw–Karma model (solid gray line) and the PWL model (dashed black line) for $T_p = 0.27$ s. All other parameter values as in Tables I–V.

III. PERIOD 1 ORBITS

A test case for any cardiac Ca^{2+} model is whether it produces regular Ca^{2+} oscillations (period 1 orbits) when driven at low pacing frequency. To establish this property for the PWL model, we start by rewriting the governing equations as $\dot{x} = Mx + f(t)$, where the dot indicates the derivative with respect to time and $x = (c_s, c_i, c_j, c_j', I_r) \in \mathbb{R}^5$. The entries

of the matrix $M \in \mathbb{R}^{5 \times 5}$ and the vector $f \in \mathbb{R}^5$ follow readily from Eq. (1) and those in Appendix B. Note that M is a piecewise constant matrix in time, whose entries only change when the dynamics passes through either a voltage or a time-dependent switch as explained in more details below. The only nonzero entries in f are at the first and the last positions, because the first entry results from the voltage dependence of
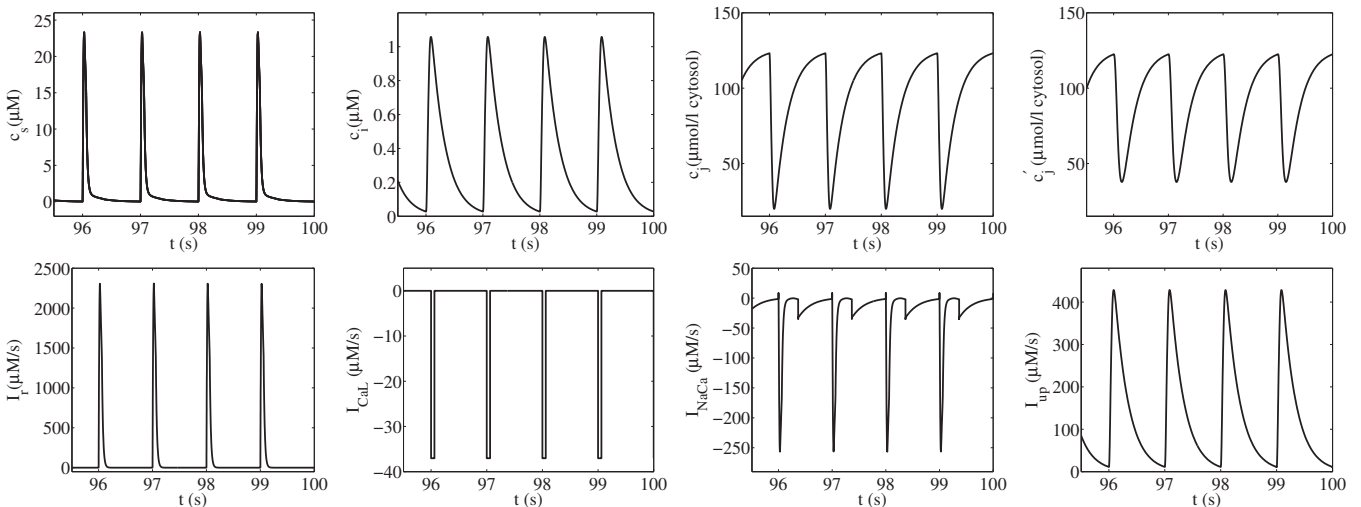

FIG. 3. Time courses of the Ca^{2+} concentration in the subsarcolemmal space (c_s), the cytosolic bulk (c_i), the total Ca^{2+} in the SR (c_j), the Ca^{2+} concentration in the unrecruited JSR (c_j'), the release current I_r, the L-type Ca^{2+} current I_{CaL}, the NCX current I_{NaCa}, and the uptake current I_{up} in the PWL model at a pacing period of $T_p = 1$ s. All other parameter values as in Tables I–IV and VI.
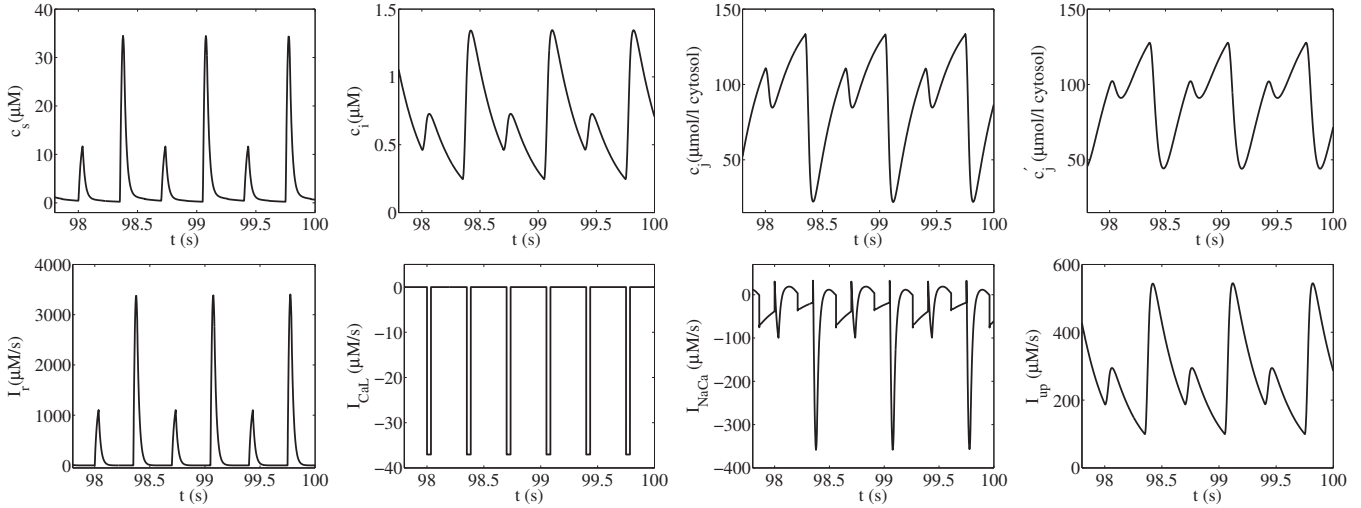
FIG. 4. Time courses of the Ca^{2+} concentration in the subsarcolemmal space (c_s), the cytosolic bulk (c_i), the total Ca^{2+} in the SR (c_j), the Ca^{2+} concentration in the unrecruited JSR (c_j'), the release current I_r, the L-type Ca^{2+} current I_{CaL}, the NCX current I_{NaCa}, and the uptake current I_{up} in the PWL model at a pacing period of $T_p = 0.35$ s. All other parameter values as in Tables I–IV and VI.

I_{NaCa}, namely, $\phi(V)$, and the last entry is controlled by the constant terms of Q as given by Eq. (A2). Since we prescribe the shape of the action potential, the voltage dependence of I_{NaCa} translates into a time dependence. When we derived the PWL model in Sec. II B, we introduced switches with respect to the membrane potential at $V = V_L$ and $V = V_{NaCa}$. Bearing in mind that the action potential is clamped, the presence of voltage thresholds means that the governing equation for a trajectory changes at times when the voltage crosses one of these switches. For a given voltage clamp, these times are fixed by the condition $V(T) = V_{th}$, where $V_{th} \in \{V_L, V_{NaCa}\}$. In addition to these voltage switches, the PWL load-release function Q introduces additional switching times that are determined by the time course of the Ca^{2+} concentration in the unrecruited JSR. Since c_j' dynamically evolves in time, these switching times are not known *a priori*, but have to be computed as part of the solution. Let $\{T_i\}_{i=1,\dots,m}$ be the set of all switching times. Given the Ca^{2+} concentrations and the release current $x_i = x(T_i)$ at the ith switching time, their values at T_{i+1} follow from

$$x_{i+1} = e^{M_i(T_{i+1}-T_i)}x_i + \int_{T_i}^{T_{i+1}} e^{M_i(T_{i+1}-s)}f(s)\mathrm{d}s, \qquad (2)$$

where M_i, $i=0,\dots,m$, is a constant matrix and we have set $T_0 = 0$ and $T_{m+1} = T_p$ for consistency. A convenient way to evaluate the integral is to diagonalize M_i, i.e., to write $M_i P_i = P_i \Lambda_i$, where the columns of P_i hold the eigenvectors of M_i and the entries of the diagonal matrix Λ_i are the corresponding eigenvalues. The integral then reduces to one-dimensional convolutions of f with an exponential function. The functional forms that we have adopted for I_{NaCa} and the voltage clamp mean that the integrals in Eq. (2) can be computed explicitly, leading to an analytical form for x_{i+1}. This leads us to the introduction of a family of closed-form propagators Z_i such that $x_{i+1} = Z_i x_i$. Any trajectory of x is classified by the sequence of switching events, either time-dependent

(voltage switches) or state-dependent (threshold crossings of c_j'). Hence, to compute a closed orbit, we need to specify the order and type of switches beforehand. Let $\{d_i\}_{i=1,\dots,n}$ denote the sequence of threshold crossings in the unrecruited JSR with yet to be determined switching times $\{T_i^s\}$, and let $\{T_j^t\}$ be the known voltage switches in time. Here, the d_i are the values of c_j' where the dynamics switch, and $d_i \in \{50, 115\}$ due to the definition of Q [see Eq. (A2)]. When we order the switching times according to the specific sequence of switching events and denote this set by Γ, e.g., $\Gamma = \{T_1^s, T_1^t, T_2^s, \dots\} = \{T_1, T_2, T_3, \dots, T_m\}$, then a period 1 orbit satisfies the conditions

$$x(0) = x(T_p) = Z_{m+1} \cdots Z_1 x(0), \qquad c_j'(T_i^s) = d_i. \qquad (3)$$

The first expression in Eq. (3) ensures periodicity with a period of T_p and $c_j'(T_i^s)$ is the fourth component of

$$x_i = Z_{i'} \cdots Z_1 x_0, \qquad (4)$$

where i' corresponds to the position of T_i^s in the ordered set Γ. Note that there are $5+n$ unknowns—the five components of the initial value vector x_0 and the n c_j' dependent switching times—and that there are exactly $5+n$ conditions. Figure 6 depicts period 1 orbits for different pacing frequencies con-
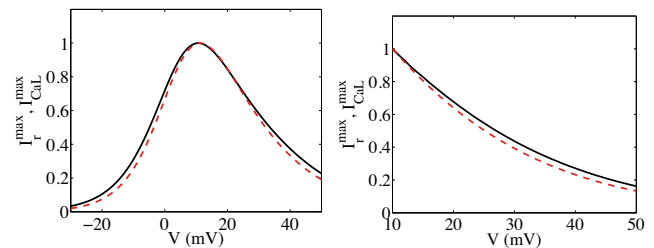

FIG. 5. (Color online) Maximal L-type current I_{CaL} (dashed) and SR current I_r (solid) for test potential steps from -80 mV to the indicated voltage in the Shiferaw–Karma model (left) and the PWL model (right). All currents are normalized to the overall maximum. All other parameter values as in Tables I–VI.
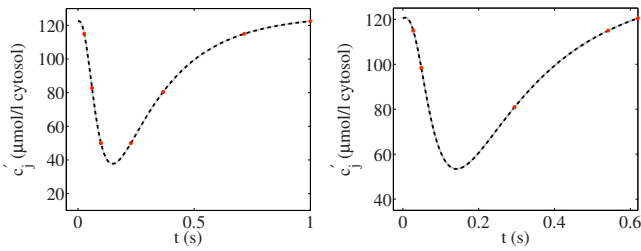
FIG. 6. (Color online) The shape of the periodic solution obtained numerically (dashed lines) and the corresponding analytical solution given by Eqs. (2) and (3) (solid lines) for $T_p = 1$ s (left) and $T_p = 0.62$ s (right). The circles indicate the concentration values at switching times. All other parameter values as in Tables I–IV and VI.
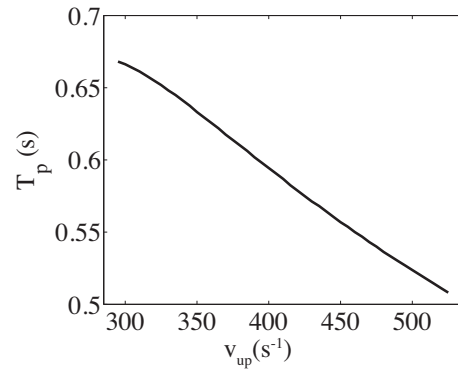

FIG. 7. Continuation of the period-doubling bifurcation as a function of the pump strength v_{up}. All other parameter values as in Tables I–IV and VI.

structed by solving Eq. (3). The solution given by Eqs. (2) and (3) is in excellent agreement with numerical simulations. The difference between the two panels lies in the number of switching times. Upon decreasing the basic cycle length, the minimum of c_j' increases, until it exceeds the threshold value of 50 μmol/l cytosol in the unrecruited JSR, which results in the loss of two switching events.

Now that we have explicitly constructed period 1 orbits, we continue by probing their linear stability. We here assume that small perturbations around the periodic orbit $x(t)$ result in shifted switching times $\tilde{T}_i = T_i + \delta T_i$, but that the order and type of the switching events remain unchanged. The last assumption is equivalent to stating that the matrices M_i still govern the dynamics between $\tilde{T}_i$ and $\tilde{T}_{i+1}$. Denoting the perturbed orbit at a perturbed switching time as $\tilde{x}_i = \tilde{x}(\tilde{T}_i)$, we find from Eq. (2) for $i = 0, \dots, m$ that

$$\tilde{x}_{i+1} = e^{M_i(\tilde{T}_{i+1} - \tilde{T}_i)} \tilde{x}_i + \int_{\tilde{T}_i}^{\tilde{T}_{i+1}} e^{M_i(\tilde{T}_{i+1} - s)} f(s) \, ds. \tag{5}$$

When we make the ansatz $\tilde{x}(\tilde{T}_i) = x_i + \delta x_i$, then linearizing Eq. (5) yields

$$
\begin{aligned}
\delta x_{i+1} &= e^{M_i(T_{i+1} - T_i)} \delta x_i + \delta T_{i+1}[M_i x_{i+1} + f(T_{i+1}^-)] \\
&\quad - \delta T_i e^{M_i(T_{i+1} - T_i)} [M_i x_i + f(T_i^+)] \\
&= e^{M_i(T_{i+1} - T_i)} [\delta x_i - \dot{x}(T_i^+) \delta T_i] + \dot{x}(T_{i+1}^-) \delta T_{i+1}, \tag{6}
\end{aligned}
$$

where we used the definition of $\dot{x}$ as introduced at the beginning of the section. The derivatives of x have to be taken either from above ($\dot{x}(T_i^+)$) or below ($\dot{x}(T_i^-)$) due to the discontinuity of f. Equation (6) possesses a direct geometrical interpretation since it states that the perturbation at $\tilde{T}_{i+1}$ results from propagating the perturbation at $\tilde{T}_i$ until T_{i+1}, and then adding the contribution from the perturbation δT_{i+1}. At first sight, Eq. (6) appears implicit as it relates the perturbation δx_{i+1} to the unknown shift in the switching time δT_{i+1}. However, we need to solve Eq. (6) subject to the threshold conditions and the fact that the basic cycle length remains unchanged. The latter condition entails that $\delta T_0 = \delta T_{m+1} = 0$. For the former, we have to distinguish between voltage-dependent and c_j' dependent switches. Since the action potential remains unchanged, we find $\tilde{T}_j^t = T_j^t$, so that $\delta T_{j'} = 0$, where j' corresponds to the position of T_j^t in the ordered set Γ. If $T_{i'}$ indicates a threshold crossing of c_j', then $\tilde{c}_j'(\tilde{T}_{i'})$

$= d_i = c_j'(T_{i'})$, so that the fourth component of $\delta x_{i'}$ vanishes. To illustrate the above procedure, we consider the evaluation of δx_1 for a c_j' dependent switch at $\tilde{T}_1$. Since $T_0 = \delta T_0 = 0$, we find from Eq. (6)

$$\delta x_1 = e^{M_0 T_1} \delta x_0 + \dot{x}(T_1^-) \delta T_1, \tag{7}$$

and hence for the fourth component of δx_1,

$$0 = \sum_{i=1}^{5} [e^{M_0 T_1}]_{4i} [\delta x_0]_i + [\dot{x}(T_1^-)]_4 \delta T_1, \tag{8}$$

which leads to

$$\delta T_1 = \sum_{i=1}^{5} [g_0]_i [\delta x_0]_i. \tag{9}$$

Here, we introduce the vector $g_0 \in \mathbb{R}^5$ with $[g_0]_i = -[e^{M_0 T_1}]_{4i} / [\dot{x}(T_1^-)]_4$, so that

$$\delta x_1 = [e^{M_0 T_1} + \dot{x}(T_1^-) g_0] \delta x_0. \tag{10}$$

Equation (10) uniquely relates the perturbations at the first perturbed switching time to the perturbation at the beginning of the action potential since all the components in the square brackets are known as they stem from the unperturbed periodic orbit. Extending the preceding analysis to all switching events, we finally arrive at a matrix S_m such that $\delta x_{m+1} = S_m \delta x_0$. The stability of the periodic orbit x then readily follows from the eigenvalues σ_i of S_m. If $|\sigma_i| < 1$ for all $i = 1, \dots, 5$, then the orbit is linearly stable. A period-doubling bifurcation occurs if there is one eigenvalue with $\sigma_j = -1$, while $|\sigma_i| < 1$ for $i \neq j$. The explicit construction of the matrix S_m allows us to directly compute the critical value of T_p for the period-doubling bifurcation by solving $\det(S_m + I_5) = 0$, where I_5 is the 5×5 identity matrix. Figure 7 shows the continuation of the period-doubling bifurcation when we vary the strength of Ca^{2+} resequestration to the SR. Upon energizing the Ca^{2+} pumps, the critical value of T_p decreases, so that the cell can be paced faster before alternans set in. The results presented in Figs. 3 and 4 are consistent with the linear stability analysis derived above as the basic cycle lengths lie on either side of the critical line in Fig. 7.
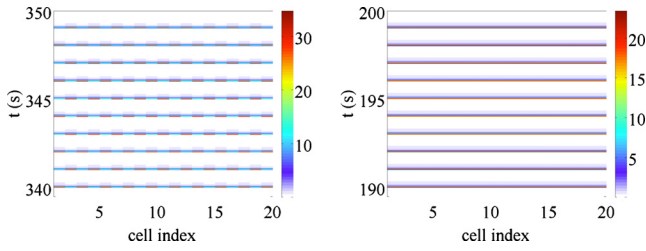
FIG. 8. (Color online) Subsarcolemmal Ca^{2+} concentration in a network of 20 cells paced at $T_p = 1$ s with a coupling strength of $\tau_c = 2$ ms (left) and $\tau_c = 3$ ms (right). All other parameter values as in Tables I–IV and VI.

IV. NETWORK DYNAMICS

In Sec. III, we explicitly constructed period 1 orbits for a single cell and probed linear stability. Here, we will investigate the dynamics of a coupled cell network, where each cell is labeled by an index μ with $\mu = 1, \ldots, N_c$. We will focus on the nearest-neighbor linear coupling of the form $\sum_{\nu \in nn} (c_i^\nu - c_i^\mu)/\tau_c$ added to the dynamics of the bulk cytosolic Ca^{2+} concentration of the μth cell. Figure 8 depicts the behavior of 20 cells in such a network. The dynamics is depicted as space time plots, where time runs vertically and space (i.e., the cell index) runs horizontally. We choose a color coding such that warm colors present high Ca^{2+} concentrations, while cooler colors indicate lower Ca^{2+} concentrations. For the sake of a clearer presentation, Ca^{2+} concentrations close to the resting level are shown in white. Hence, each colored line in Fig. 8 corresponds to the subsarcolemmal Ca^{2+} concentration across the network responding to an action potential. For weak coupling as depicted in the right panel, all the cells synchronize (as can be seen from the solid line at each action potential onset), while increasing the coupling strength leads to spatial alternans where neighboring cells oscillate out of phase (note the alternating coloring upon stimulation). Figure 9 provides more details by displaying the time courses of individual cells. For the stronger coupling, the dynamics of neighboring cells is indeed shifted by one pacing period, which results in next nearest neighbors to follow exactly the same time traces. The right panel illustrates that the synchronous network state is identical to the orbit of a single cell at the same pacing frequency. Note that isolated cells do not exhibit alternans at the chosen basic cycle length, so that the emergence of spatial alternans results solely from the coupling.
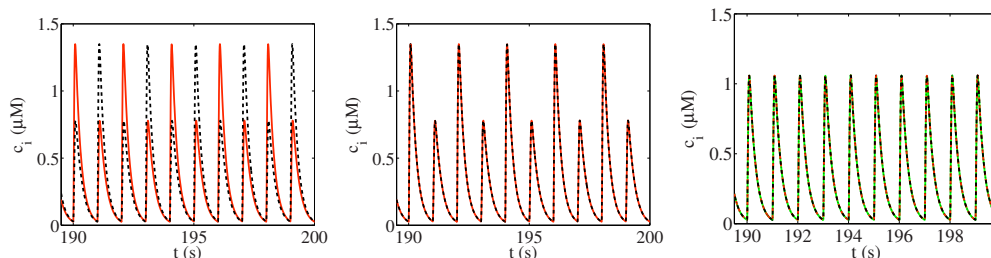
To understand this behavior, we perform a linear stability analysis of the coupled network. Then, the dynamics of an individual cell between the ith and $(i+1)$th switching events is given by

$$\dot{x}_i^\mu = [M_i x_i^\mu + f_i] \Theta(t - T_i^\mu) \Theta(T_{i+1}^\mu - t)$$
$$+ \frac{1}{\tau_c} \sum_{m,\alpha} G_{\mu\alpha} H x_m^\alpha \Theta(t - T_m^\alpha) \Theta(T_{m+1}^\alpha - t), \quad (11)$$

where Θ is the Heaviside step function with $\Theta(x) = 1$ for $x \geq 0$ and zero otherwise. The matrix $G \in \mathbb{R}^{N_c \times N_c}$ reflects the topology and the kind of coupling in the network, while $H \in \mathbb{R}^{5 \times 5}$ specifies the components of x_i through which the coupling occurs. Since we here focus on diffusive coupling in a linear array of cells, G is the usual tridiagonal matrix (discretized Laplacian) modified to satisfy either no-flux or periodic boundary conditions. The only nonzero element in H is H_{22} since the bulk Ca^{2+} concentration in one cell couples to the bulk Ca^{2+} concentration in the neighboring cells. The sum over m stems from the fact that although Eq. (11) describes the dynamics of the μth cell between T_i^μ and T_{i+1}^μ, other cells can follow different switching patterns and hence have different switching times. A synchronous state is one for which all cells follow a common trajectory with the same phase, $x^\mu(t) = x(t) \ \forall \mu$. Using the same notations and assumptions as in Sec. III, we find for the linearized dynamics around the synchronous network state $s(t)$ [with $x(t)$ the periodic orbit of the uncoupled cell described in Sec. III],

$$\frac{d}{dt} \delta x_i^\mu = M_i \delta x_i^\mu \Theta(t - T_i) \Theta(T_{i+1} - t)$$
$$+ \dot{s}_i [\delta T_{i+1}^\mu \delta(t - T_{i+1}) - \delta T_i^\mu \delta(t - T_i)]$$
$$+ \frac{1}{\tau_c} \sum_{j,\alpha} G_{\mu\alpha} H \{ \delta x_j^\alpha \Theta(t - T_j) \Theta(T_{j+1} - t)$$
$$+ s_j [\delta T_{j+1}^\alpha \delta(t - T_{j+1}) - \delta T_j^\alpha \delta(t - T_j)] \}. \quad (12)$$

Here, $s_i(t)$ refers to the value of $s(t)$ for $T_i < t < T_{i+1}$. Note that the switching times that appear in the Heaviside and delta functions do not carry a cell index anymore, since these times belong to the synchronous network state where all cells switch dynamics at the same time. To solve Eq. (12), we employ ideas originally developed by Pecora and Carroll (1998). Let $\mathcal{Q}$ denote the matrix whose columns correspond to the eigenvectors of the connectivity matrix G, and let Ω be

FIG. 9. (Color online) Bulk Ca^{2+} concentration for two neighboring cells (left, right) and two second neighbor cells (middle) for $\tau_c = 1$ ms (left, middle) and $\tau_c = 3$ ms (right) in a network of 20 cells paced at $T_p = 1$ s. The additional trace in the right panel results from the simulation of an isolated cell at the same parameter values. All other parameter values as in Tables I–IV and VI.
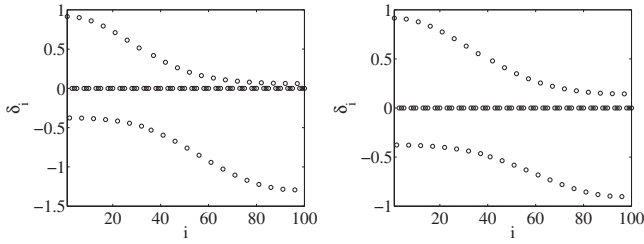
FIG. 10. Eigenvalues of the linearized dynamics for a network of 20 cells paced at $T_p = 1$ s with a coupling strength of $\tau_c = 2$ ms (left) and $\tau_c = 3$ ms (right). Note that there are $5N_{cell}$ eigenvalues. All other parameter values as in Tables I–IV and VI.

a diagonal matrix that holds all the eigenvalues γ_ν of G. When we introduce the new variable $\delta y_i^\nu = \sum_\mu \mathcal{Q}_{\nu\mu}^{-1} \delta x_i^\mu$, we find, e.g., for the first sum in Eq. (12)

$$\sum_{\mu,j,\alpha} \mathcal{Q}_{\nu\mu}^{-1} G_{\mu\alpha} H \delta x_j^\alpha \Theta(t - T_j)\Theta(T_{j+1} - t)$$
$$= \gamma_\nu \sum_j H \delta y_j^\nu \Theta(t - T_j)\Theta(T_{j+1} - t) \quad (13)$$

due to $\mathcal{Q}^{-1} G = \Omega \mathcal{Q}^{-1}$. Rewriting Eq. (12) in terms of δy_i^ν then results in

$$\frac{d}{dt}\delta y_i^\nu = M_i \delta y_i^\nu \Theta(t - T_i)\Theta(T_{i+1} - t)$$
$$+ \dot{s}_i[\delta U_{i+1}^\nu \delta(t - T_{i+1}) - \delta U_i^\nu \delta(t - T_i)]$$
$$+ \frac{\gamma_\nu}{\tau_c}\sum_j H\{\delta y_j^\nu \Theta(t - T_j)\Theta(T_{j+1} - t)$$
$$+ s_j[\delta U_{j+1}^\nu \delta(t - T_{j+1}) - \delta U_j^\nu \delta(t - T_j)]\}, \quad (14)$$

where we introduce $\delta U_i^\nu = \sum_\mu \mathcal{Q}_{\nu\mu}^{-1} \delta T_i^\mu$. Equation (14) depends only on one cell index ν. All the information on the network topology and on the kind of coupling is encoded in the eigenvalues γ_ν, which are, e.g., given by $\gamma_\nu = -4\sin^2(\pi(\nu-1)/N_c)$ in the case of periodic boundary conditions. For $\nu = 1$, $\gamma_1 = 0$, and so the network stability is determined in part by the stability of the uncoupled single cell periodic orbit. For $\nu \neq 1$, all other eigenvectors correspond to transverse directions (and eigenfunctions are discrete sin and cos functions of the cell indices). Bearing in mind that we
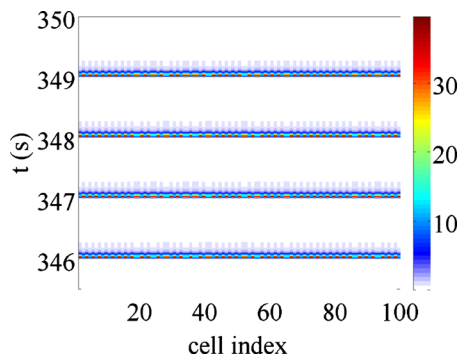

FIG. 11. (Color online) Subsarcolemmal Ca^{2+} concentration in a network of 100 cells paced at $T_p = 1$ s with a coupling strength of $\tau_c = 1$ ms. All other parameter values as in Tables I–IV and VI.
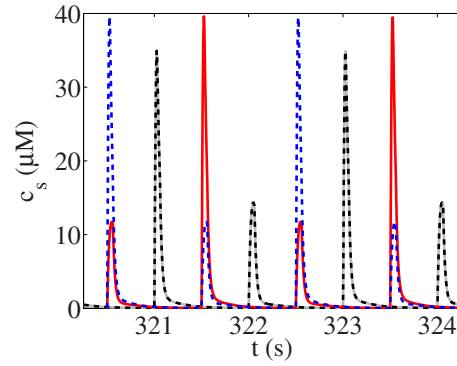

FIG. 12. (Color online) Subsarcolemmal Ca^{2+} concentration in a network of 100 cells for two neighboring cells that are synchronized (solid gray and dashed black lines) and that oscillate out of phase (solid red and dashed blue lines). The profiles of the two pairs of cells are plotted with a shift of half a period with respect to each other for better illustration. Parameter values as in Fig. 11.

need to integrate Eq. (14) between $T_i + \delta U_i^\nu$ and $T_{i+1} + \delta U_{i+1}^\nu$, we find to first order that

$$\delta y_{i+1}^\nu = e^{R_i^\nu(T_{i+1} - T_i)}[\delta y_i^\nu - p_i^\nu \delta U_i^\nu] + q_{i+1}^\nu \delta U_{i+1}^\nu, \quad (15)$$

with $R_i^\nu = M_i + \gamma_\nu H / \tau_c$, $p_i^\nu = \dot{s}(T_i^+) + \gamma_\nu H s_i / \tau_c$, and $q_i^\nu = \dot{s}(T_i^-) + \gamma_\nu H s_i / \tau_c$. Equation (15) possesses the same structure as Eq. (6) for the uncoupled cell—the two equations coincide for $\gamma_\nu = 0$—so the technique of stability analysis that we developed in Sec. III carries over to the network. We therefore introduce matrices S_m^ν that are defined by $\delta y_{i+1}^\nu = S_m^\nu \delta y_i^\nu$ and that have eigenvalues σ_j^ν. Since δx_i^μ and δy_i^ν are linearly related, any instability of δy_i^ν corresponds to an instability of the original network dynamics. If $|\sigma_j^\nu| < 1$ for all ν and j, then the synchronous network state is linearly stable. If, on the other hand, there is one eigenvalue in $\{\sigma_j^\nu\}$ with the value of -1, while all other eigenvalues lie within the unit circle around the origin of the complex plane, then the network undergoes a period-doubling bifurcation. In Fig. 10, we plot the eigenvalues for the network dynamics shown in Fig. 8. For the stable synchronous state, all eigenvalues have moduli smaller than 1, while the presence of the spatial alternans is accompanied by some eigenvalues with $\sigma_j^\nu < -1$. Note that all eigenvalues are smaller than 1, so the instability indeed occurs through a period-doubling bifurcation. The onset of the instability depends on the number of cells in the network since the eigenvalues γ_ν depend on N_c. In addition, larger networks can display spatially irregular alternans where most cells oscillate out of phase with respect to their neighbors, while some adjacent cells are perfectly synchronized. An example for this kind of dynamics is depicted in Fig. 11. Here, there are 11 pairs of neighboring cells that oscillate in phase. Figure 12 reveals that synchronized neighboring cells possess different maxima than adjacent cells that oscillate out of phase with respect to each other.

V. DISCUSSION

Understanding the genesis of cellular alternans is a key factor in controlling and treating arrhythmia in the heart given the strong evidence that links these two phenomena (Myles *et al.*, 2008; Laurita and Rosenbaum, 2008). At the

level of single cells, two kinds of alternans exist, which manifest themselves as beat-to-beat variations in the membrane potential and in the Ca^{2+} concentration, respectively. Due to the bidirectional coupling between the voltage and the Ca^{2+} dynamics, these two forms of alternans often occur simultaneously. However, studies *in vitro* (Chudin *et al.*, 1999) and *in vivo* (Aistrup *et al.*, 2006) have shown that Ca^{2+} alternans occur in the absence of variations in the action potential. This has led to the notion that the Ca^{2+} subsystem undergoes an instability before the membrane potential passes through a bifurcation, and hence might be the driving force behind arrhythmia. Consequently, experimental and theoretical studies have extensively probed the response of the intracellular Ca^{2+} dynamics to a clamped action potential. In the present work, we followed up on this idea and developed a novel mathematically tractable model of the intracellular Ca^{2+} subsystem that is driven by a predefined action potential.

Our starting point is the Shiferaw–Karma model (Shiferaw *et al.*, 2003), where Ca^{2+} cycles through two cytosolic and two luminal compartments. The coupling of the membrane potential to the Ca^{2+} dynamics occurs through the L-type Ca^{2+} channel and the NCX, where both currents, I_{CaL} and I_{NCX}, are nonlinear functions of the Ca^{2+} concentration and the membrane potential. In the first step, we replaced all nonlinearities by state-dependent switches, so that the dynamics becomes PWL with a time-dependent drive. Importantly, our model reproduces the behavior of the original Shiferaw–Karma model in that it shows, e.g., a period-doubling bifurcation upon increasing the pacing frequency and the crucial characteristics of graded release and gain. We also recover the multiphase time course of the NCX current. The identification of appropriate switching times that signal the change from one set of linear evolution equations to another one suggests that the fundamental dynamics do not rely so much on the biophysical details, but more on the overall characteristics. This notion is also supported by the fact that we could replace functions (originally arising from a fast buffer approximation) in the bulk and in the subsarcolemmal space by two constants, with negligible effects on the dynamics. One drawback of our current model is that it does not allow for Ca^{2+}-induced inactivation of the L-type Ca^{2+} channel, and hence excludes the L-type Ca^{2+} channel as a mechanism to induce alternans. However, this is a subject of ongoing research and will be discussed elsewhere.

The PWL nature of our model allows us to explicitly construct the periodic orbits of the intracellular Ca^{2+} concentrations with no need to resort to numerical simulations. In turn, this opens up the avenue for efficiently scanning the response of the Ca^{2+} dynamics to changes in physiologically relevant parameters such as the pacing frequency, the pump strength, or the load-release function. The analytic solutions for the Ca^{2+} dynamics immediately lead to an expression for the linear stability of periodic 1 orbits. This removes any need to reduce the dimensions of the original dynamical system by assuming, e.g., equality of the Ca^{2+} concentration in the two cytosolic and luminal compartments at the beginning of an action potential, respectively, as has been done in previous analyses of the Shiferaw–Karma model (Shiferaw

et al., 2003; Restrepo and Karma, 2009), or quasistationarity of some of the Ca^{2+} concentrations (Huertas *et al.*, 2010). The specific form of the matrix S_m that contains all the information about the linear stability depends on the kind of switches, i.e., time- or state-dependent, and their relative order. We explicitly demonstrated how to analyze a time-dependent switch followed by a state-dependent switch. The generalization of this procedure is straightforward, so that the linear stability analysis presented here holds for any driven PWL system with an arbitrary number and sequence of switching events. The expression for the linear stability allows us to continue the period-doubling bifurcation that signals the onset of Ca^{2+} alternans. We find that upon energizing Ca^{2+} pumps, the critical frequency for the onset of Ca^{2+} alternans increases. Given that the main mechanism to induce Ca^{2+} alternans in the current model is a depletion of the SR (Sipido, 2004), these results are consistent with the physiological role of Ca^{2+} pumps since stronger pumps allow a faster replenishment of the SR, so that cells can be driven harder before depletion occurs. Similar findings were reported earlier in experimental and theoretical studies based on more elaborate models (Shiferaw *et al.*, 2003; Xie *et al.*, 2008).

After constructing and probing the linear stability of regular Ca^{2+} orbits in a single cell, we investigated the behavior of a coupled cell network. A linear array of cells that are coupled diffusively through the bulk cytosolic Ca^{2+} concentration exhibits alternans at a pacing frequency when a single cell still oscillates with a period equal to the pacing period. These spatial alternans hence derive from the coupling, since decreasing the coupling strength promotes a linearly stable synchronous state where all cells follow the same trajectories. We base our linear stability analysis of the network state on work by Pecora and Carroll (1998). All the information about the topology and the kind of coupling enters through altered coefficients in the single cell equation, so that the whole linear stability analysis generalizes from isolated cells to networks. We find a period-doubling bifurcation of the network state that explains why the network shows beat-to-beat variations in the intracellular Ca^{2+} concentration, while a single cell still oscillates regularly. The critical value of the basic cycle length below which alternans exist depends on the size of the network, so do the patterns that emerge when the pacing frequency is increased. For a network of 100 cells, we observe, e.g., almost regular spatial alternans interspersed with groups of two cells that are synchronized.

So far, we have referred to the Shiferaw–Karma and PWL models as single cell descriptions. This is justified in ventricular myocytes where the Ca^{2+} dynamics is known to oscillate homogeneously in space so that a whole cell description in terms of ordinary differential equations holds true. Hence, coupling these equations corresponds to investigating the dynamics of ventricular cardiac muscle tissue. On the other hand, the Shiferaw–Karma and PWL models can be interpreted as the dynamics at a single dyadic cleft. Since the t-tubule system in ventricular myocytes guarantees that L-type Ca^{2+} channels always juxtapose Ca^{2+} release channels on the SR, coupling Eq. (1) then mimics the dy-

namics of a single cell. Intracellular spatial alternans have been observed experimentally (Cordeiro *et al.*, 2007; Gaeta *et al.*, 2009) and investigated theoretically using networks of Shiferaw–Karma models (with nearest-neighbor coupling in c_s and c_j and the inclusion of a voltage dynamics using a current balance equation) (Echebarria and Karma, 2002; Shiferaw and Karma, 2006; Zhao, 2008; Dai and Schaeffer, 2010). For atrial myocytes that lack t-tubules, a multiple node view as adapted above fails due to the spatial heterogeneity of intracellular Ca^{2+} concentration profiles. Since nonjunctional release sites in atrial myocytes are not exposed to L-type Ca^{2+} currents, Eq. (1) only corresponds to the dynamics at junctional release sites, so that the coupled model does not capture the morphology of an isolated atrial myocyte either. Nevertheless, intracellular Ca^{2+} alternans have been observed in atrial myocytes (Kockskämper and Blatter, 2002; Blatter *et al.*, 2003), and so the development of an appropriate model is an open challenge. Adapting our present framework to understand the emergence of beat-to-beat variations in atrial myocytes is a natural next step.

The insight that whole heart arrhythmia strongly correlates with cellular alternans has sparked the idea to build cardiac models that incorporate all the dynamics from the subcellular to the tissue level, especially in the light of possible therapies. This presents one of the greatest challenges in the cardiac modeling community, and to date, most results have been obtained for a specific dynamical level. For example, a significant amount of work is dedicated to understand a detailed single cell behavior, while at the tissue level, these details are generally integrated out in favor of understanding larger scale phenomena. The reason for such a division lies in the fact that cardiac dynamics spans multiple scales both in space and time, ranging from nanometer to centimeter and from milliseconds to days. Possible candidates to bridge this gap are homogenization techniques (Higgins *et al.*, 2007), ideas from hierarchical dynamical systems (Thul and Falcke, 2007; Leonhardt *et al.*, 2008), or high performance numerical simulations (Clayton *et al.*, 2010).

Advances in imaging techniques have revealed intracellular heterogeneities. To study the impact of space dependent changes in, e.g., Ca^{2+} pumps or L-type Ca^{2+} channels requires a generalization of the framework presented here, especially with respect to the linear stability analysis. Furthermore, there is now strong evidence for the impact of molecular fluctuations on cellular patterns. Some of the work on cardiac alternans already explicitly represents the stochastic behavior of Ca^{2+} release channels through Markov chain models (Restrepo and Karma, 2009; Huertas *et al.*, 2010). However, these studies rely heavily on numerical simulations. To develop models that offer the same depths of mathematical analysis as in the present work, while accounting for cellular fluctuations, would provide us with a framework to study PWL random dynamical systems, while at the same time shed more light on the emergence of Ca^{2+} alternans, and hence contribute to the treatment of cardiac arrhythmia. We are currently developing such ideas based around the use of stochastic fire-diffuse-fire models (Coombes and Timofeeva, 2003).

TABLE I. Physical constants and external concentrations in the Shiferaw–Karma model.

	Definition	Value
T	Temperature	308 K
F	Faraday's constant	96.4867 C/mmol
R	Gas constant	8.314 J/K mol
Na_o	External sodium concentration	140 mM
Ca_o	External calcium concentration	1.8 mM
v_s/v_i	Subsarcolemmal/cell volume	0.1

APPENDIX A: SHIFERAW–KARMA MODEL

Here, we give some details of the original Shiferaw–Karma model collected from Shiferaw *et al.* (2003), (2005) and Shiferaw and Karma (2006). The function $\beta = \beta(c)$ arises from the fast buffer approximation and takes the form

$$\beta(c) = \frac{1}{1 + \dfrac{B_{SR}K_{SR}}{(c + K_{SR})^2} + \dfrac{B_{Cd}K_{Cd}}{(c + K_{Cd})^2} + \dfrac{B_T K_T}{(c + K_T)^2}}. \quad (A1)$$

The load-release function $Q = Q(c_j')$ is given by the PWL function

$$Q(c_j') = 10^{-3} \begin{cases} 0, & 0 \le c_j' < 50 \\ c_j' - 50, & 50 \le c_j' < 115 \\ uc_j' + s, & c_j' \ge 115, \end{cases} \quad (A2)$$

where u measures the steep nonlinear dependence of Ca^{2+} release on the SR Ca^{2+} concentration, and s is a constant that is chosen such that Q is continuous. The current through the NCX is

$$I_{NaCa} = \bar{I}_{NaCa} \frac{\eta Na_i^3 Ca_o - \eta e^{-\alpha} Na_o^3 \tilde{c}_s}{(K_{mNa}^3 + Na_o^3)(K_{mCa} + Ca_o)}, \quad (A3)$$

with

$$\eta = \frac{e^{\xi\alpha}}{1 + k_{sat}e^{(\xi-1)\alpha}}, \quad (A4)$$

where $\alpha = FV/RT$ and $\tilde{c}_s = c_s \times 10^{-3}$. The internal Na concentration is set to

$$Na_i(T_p) = \frac{a_N}{1 + b_N\sqrt{T_p}}, \quad a_N = 28, \ b_N = 10. \quad (A5)$$

For the current through the L-type Ca^{2+} channel, we here only mention the single channel current, which is given by

$$i_{CaL} = 4\alpha \bar{i}_{Ca} F P_{Ca} \frac{c_s \exp(2\alpha) - \gamma_o Ca_o}{\exp(2\alpha) - 1}. \quad (A6)$$

Note that I_{CaL} is negative and is built from i_{CaL} using the prescription in Shiferaw *et al.* (2003). The Ca^{2+} uptake current $I_{up} = I_{up}(c_i)$ is given by the Hill function

TABLE II. Parameter values for the NaCa exchanger and the SR uptake in the Shiferaw–Karma model with other values from Luo and Rudy (1994).

	Definition	Value
c_{up}	Uptake threshold	0.5 μM
v_{up}	Uptake strength	270 μM/s
$\bar{I}_{NaCa}$	Strength of the NaCa exchanger	10^5 μM/s
k_{sat}	Constant from the 1994 Luo–Rudy model	0.1
ξ	Constant from the 1994 Luo–Rudy model	0.35
K_{mNa}	Constant from the 1994 Luo–Rudy model	87.5 mM
K_{mCa}	Constant from the 1994 Luo–Rudy model	1.38 mM
γ_s	Constant from the 1994 Luo–Rudy model	1
γ_o	Constant from the 1994 Luo–Rudy model	0.341

$$I_{up} = \frac{v_{up}c_i^2}{c_{up}^2 + c_i^2}. \qquad (A7)$$

The clamped action potential follows the temporal shape

$$V(t) = \begin{cases} V_+(t), & mT_p \le t < (m+x)T_p \\ V_{min}, & (m+x)T_p \le t < (m+1)T_p, \end{cases} \qquad (A8)$$

where

$$V_+(t) = V_{min} + \Delta V \sqrt{1 - \left(\frac{t - mT_p}{xT_p}\right)^2}, \qquad (A9)$$

and $\Delta V = (V_{max} - V_{min})$. Here, V_{min} and V_{max} denote the minimal and maximal values of the action potential, respectively, and the APD is given by

$$x(T_p) = \frac{a_x}{a_x + T_p}, \quad a_x = 2/3. \qquad (A10)$$

In Tables I–V, we list all the parameter values of the Shiferaw–Karma model, even those that we have not discussed above, but which are essential for simulating the model such as for the gating dynamics of the L-type Ca^{2+} channel.

APPENDIX B: PWL MODEL

Here, we give the details of the PWL model. Using the same notation as in Appendix A, this is defined by the system of Eq. (1) with $\beta(c_s)$ replaced by β_s, $\beta(c_i)$ replaced by

TABLE III. Parameter values for the L-type Ca^{2+} channel in the Shiferaw–Karma model.

	Definition	Value
P_{Ca}	Constant from the 1994 Luo–Rudy model	5.4×10^{-4} cm/s
$\bar{i}_{Ca}$	Flux constant	11 000 μmol/C cm
τ_f	Time constant for voltage-dependent inactivation	30 ms
τ_{fCa}	Time constant for calcium dependent inactivation	20 ms
$\tilde{c}_c$	Calcium inactivation threshold	0.5 μM
γ_L	Sensitivity parameter for calcium dependent inactivation	1

TABLE IV. Parameter values for the SR release in the Shiferaw–Karma model.

	Definition	Value
g	Release current strength	3×10^4 sparks/μM
u	Release slope	11.3 s^{-1}
τ_r	Average spark life time	20 ms
τ_a	Relaxation time of c_j' to c_j	50 ms
τ_s	Submembrane diffusion time constant	10 ms

β_i, and $I_{up} = v_{up}c_i$. We model the L-type Ca^{2+} current as $I_{CaL} = \Theta(V - V_L)i_{CaL}$ with the threshold voltage $V_L = V_{max} - 1$ and a constant conductance

$$i_{CaL} = -\bar{i}_{Ca}P_{Ca}\frac{a_{CaL}F\gamma_o Ca_o}{\exp(2a_{CaL}) - 1}, \qquad (B1)$$

where $a_{CaL} = V_{max}F/RT$. The current through the NCX is given by $I_{NaCa} = \phi(V) - \psi(V)c_s$, where

$$\phi = \bar{I}_{NaCa}\frac{\eta_q Na_i^3 Ca_o}{(K_{mNa}^3 + Na_o^3)(K_{mCa} + Ca_o)}, \qquad (B2)$$

$$\psi = \bar{I}_{NaCa}\frac{\gamma_{NaCa}Na_o^3 \times 10^{-3}}{(K_{mNa}^3 + Na_o^3)(K_{mCa} + Ca_o)}. \qquad (B3)$$

Here, we introduce the piecewise constant function

$$\gamma_{NaCa} = \begin{cases} 0.45, & V > V_{NaCa} \\ 4, & V \le V_{NaCa}, \end{cases} \qquad (B4)$$

which switches at a threshold voltage of $V_{NaCa} = -50$ mV. The function η_q is a quadratic fit to the function η in Eq. (A4) and reads as

$$\eta_q = 0.0501\alpha^2 + 0.3816\alpha + 0.9182, \qquad (B5)$$

with α as in Appendix A. For the action potential, we expand the square root dependence in Eq. (A9) for $0 \le t \le xT_p$ as

$$V_K(t) = \sqrt{1 - \left(\frac{t}{xT_p}\right)^2} = \sum_{m=0}^{\infty} a_m \cos\left(\frac{m\pi}{2xT_p}t\right). \qquad (B6)$$

Since the right-hand side is $4T_p$ periodic, the coefficients a_m are determined by

TABLE V. Parameter values for buffering in the Shiferaw–Karma model.

	Definition	Value
B_T	Total concentration of troponin C	70 μmol/1 cytosol
B_{SR}	Total concentration of SR binding sites	47 μmol/1 cytosol
B_{Cd}	Total concentration of calmodulin binding sites	24 μmol/1 cytosol
K_{SR}	Dissociation constant for SR binding sites	0.6 μM
K_{Cd}	Dissociation constant for calmodulin binding sites	7 μM
K_T	Dissociation constant for troponin C binding sites	0.6 μM

TABLE VI. Modified parameter values for the L-type Ca^{2+} channel, the SR uptake, and the release current in the PWL model.

Parameter	Definition	Value
$\bar{i}_{Ca}$	Flux constant	2200 $\mu mol/C\,cm$
v_{up}	Uptake strength	405 s^{-1}
g	Release current strength	3.5×10^4 sparks$/\mu M$
β_s	Buffering constant for c_s	0.5
β_i	Buffering constant for c_i	0.01

$$a_m = \frac{1}{2xT_p} \int_{-2T_p}^{2T_p} V_s(t)\cos\left(\frac{m\pi}{2xT_p}t\right)dt, \tag{B7}$$

where V_s is the symmetric extension of V_K on $[-2xT_p, 2xT_p]$, i.e.,

$$V_s = \begin{cases} V_K(-2xT_p - t), & -2xT_p \le t < -xT_p \le t \\ V_K(t), & -xT_p \le t < xT_p \le t \\ V_K(2xT_p - t), & xT_p \le t < 2xT_p \le t. \end{cases} \tag{B8}$$

Unless stated otherwise, we use the same parameter values as for the Shiferaw–Karma model, while Table VI lists the new and altered parameter values.

Aistrup, G. L., Kelly, J. E., Kapur, S., Kowalczyk, M., Sysman-Wolpin, I., Kadish, A. H., and Wasserstrom, J. A., "Pacing-induced heterogeneities in intracellular Ca^{2+} signaling, cardiac alternans, and ventricular arrhythmias in intact rat heart," Circ. Res. **99**, E65–E73 (2006).

Beeler, G. W. and Reuter, H., "Reconstruction of the action potential of ventricular myocardial fibers," J. Physiol. (London) **268**, 177–210 (1977).

Bers, D. M., "Cardiac excitation-contraction coupling," Nature (London) **415**, 198–205 (2002).

Blatter, L., Kockskämper, J., Sheehan, K., Zima, A., Hüser, J., and Lipsius, S., "Local calcium gradients during excitation-contraction coupling and alternans in atrial myocytes," J. Physiol. (London) **546**, 19–31 (2003).

Cannell, M. B., Cheng, H., and Lederer, W. J., "The control of calcium release in heart muscle," Science **268**, 1045–1049 (1995).

Cheng, H., Lederer, W. J., and Cannell, M. B., "Calcium sparks: Elementary events underlying excitation-contraction coupling in heart muscle," Science **262**, 740–744 (1993).

Chudin, E., Goldhaber, J., Garfinkel, A., Weiss, J., and Kogan, B., "Intracellular Ca^{2+} dynamics and the stability of ventricular tachycardia," Biophys. J. **77**, 2930–2941 (1999).

Clayton, R., Bernus, O., Cherry, E., Dierckx, H., Fenton, F., Mirabella, L., Panfilov, A., Sachse, F., Seemann, G., and Zhang, H., "Models of cardiac tissue electrophysiology: Progress, challenges and open questions," Prog. Biophys. Mol. Biol. (in press).

Coombes, S., "The effect of ion pumps on the speed of travelling waves in the fire-diffuse-fire model of Ca^{2+} release," Bull. Math. Biol. **63**, 1–20 (2001).

Coombes, S. and Timofeeva, Y., "Sparks and waves in a stochastic fire-diffuse-fire model of calcium release," Phys. Rev. E **68**, 021915 (2003).

Cordeiro, J. M., Malone, J. E., Diego, J. M. D., Scornik, F. S., Aistrup, G. L., Antzelevitch, C., and Wasserstrom, J. A., "Cellular and subcellular alternans in the canine left ventricle," Am. J. Physiol. Heart Circ. Physiol. **293**, H3506–H3516 (2007).

Dai, S. and Schaeffer, D. G., "Chaos for cardiac arrhythmias through a one-dimensional modulation equation for alternans," Chaos **20**, 023131 (2010).

Echebarria, B. and Karma, A., "Instability and spatiotemporal dynamics of alternans in paced cardiac tissue," Phys. Rev. Lett. **88**, 208101 (2002).

Fenton, F. H. and Cherry, E. M., "Models of cardiac cell," Scholarpedia **3**, 1868 (2008).

Gaeta, S. A., Bub, G., Abbott, G. W., and Christini, D. J., "Dynamical mechanism for subcellular alternans in cardiac myocytes," Circ. Res. **105**, 335–342 (2009).

Higgins, E. R., Goel, P., Puglisi, J. L., Bers, D. M., Cannell, M., and Sneyd, J., "Modelling calcium microdomains using homogenisation," J. Theor. Biol. **247**, 623–644 (2007).

Huertas, M. A., Smith, G. D., and Györke, S., "Ca^{2+} alternans in a cardiac myocyte model that uses moment equations to represent heterogeneous junctional SR Ca^{2+}," Biophys. J. **99**, 377–387 (2010).

Jordan, P. N. and Christini, D. J., "Characterizing the contribution of voltage- and calcium-dependent coupling to action potential stability: Implications for repolarization alternans," Am. J. Physiol. Heart Circ. Physiol. **293**, H2109–H2118 (2007).

Kockskämper, J. and Blatter, L., "Subcellular Ca^{2+} alternans represents a novel mechanism for the generation of arrhythmogenic Ca^{2+} waves in cat atrial myocytes," J. Physiol. (London) **545**, 65–79 (2002).

Laurita, K. R. and Rosenbaum, D. S., "Cellular mechanisms of arrhythmogenic cardiac alternans," Prog. Biophys. Mol. Biol. **97**, 332–347 (2008).

Leonhardt, H., Zaks, M., Falcke, M., and Schimansky-Geier, L., "Stochastic hierarchical systems: Excitable dynamics," J. Biol. Phys. **34**, 521–538 (2008).

Luo, C. and Rudy, Y., "A dynamic model of the cardiac ventricular action potential. I. Simulations of ionic currents and concentration changes," Circ. Res. **74**, 1071–1096 (1994).

Luo, C. H. and Rudy, Y., "A model of the ventricular cardiac action potential, depolarization, repolarization and their interaction," Circ. Res. **68**, 1501–1526 (1991).

Matthes, J. and Herzig, S., "Less is more, or enough is enough? Ca^{2+}-dependent inactivation revisited," J. Physiol. (London) **588**, 15–16 (2010).

McKean, H. P., "Nagumo's equation," Adv. Math. **4**, 209–223 (1970).

Myles, R. C., Burton, F. L., Cobbe, S. M., and Smith, G. L., "The link between repolarisation alternans and ventricular arrhythmia: Does the cellular phenomenon extend to the clinical problem?," J. Mol. Cell. Cardiol. **45**, 1–10 (2008).

Noble, D., "A modification of the Hodgkin-Huxley equations applicable to Purkinje fibre action and pacemaker potentials," J. Physiol. (London) **160**, 317–352 (1962).

Noble, D., "Modeling the heart," Physiology **19**, 191–197 (2004).

Pecora, L. M. and Carroll, T. L., "Master stability functions for synchronized coupled systems," Phys. Rev. Lett. **80**, 2109 (1998).

Qu, Z. and Weiss, J. N., "The chicken or the egg? Voltage and calcium dynamics in the heart," Am. J. Physiol. Heart Circ. Physiol. **293**, H2054–H2055 (2007).

Restrepo, J. G. and Karma, A., "Spatiotemporal intracellular calcium dynamics during cardiac alternans," Chaos **19**, 037115 (2009).

Shiferaw, Y. and Karma, A., "Turing instability mediated by voltage and calcium diffusion in paced cardiac cells," Proc. Natl. Acad. Sci. U.S.A. **103**, 5670–5675 (2006).

Shiferaw, Y., Sato, D., and Karma, A., "Coupled dynamics of voltage and calcium in paced cardiac cells," Phys. Rev. E **71**, 021903 (2005).

Shiferaw, Y., Watanabe, M. A., Garfinkel, A., Weiss, J. N., and Karma, A., "Model of intracellular calcium cycling in ventricular myocytes," Biophys. J. **85**, 3666–3686 (2003).

Sipido, K. R., "Understanding cardiac alternans: The answer lies in the Ca^{2+} store," Circ. Res. **94**, 570–572 (2004).

Thul, R. and Falcke, M., "Waiting time distributions for clusters of complex molecules," Europhys. Lett. **79**, 38003 (2007).

Trafford, A., Diaz, M., and Eisner, D., "Coordinated control of cell Ca^{2+} loading and triggered release from the sarcoplasmic reticulum underlies the rapid inotropic response to increased L-type Ca^{2+} current," Circ. Res. **88**, 195–201 (2001).

Xie, L.-H., Sato, D., Garfinkel, A., Qu, Z., and Weiss, J. N., "Intracellular Ca alternans: Coordinated regulation by sarcoplasmic reticulum release, uptake, and leak," Biophys. J. **95**, 3100–3110 (2008).

Zhao, X., "Indeterminacy of spatiotemporal cardiac alternans," Phys. Rev. E **78**, 011902 (2008).